Received 15 October 2024; revised 6 May 2025; accepted 3 June 2025.
Date of publication 6 June 2025; date of current version 13 June 2025.

Digital Object Identifier 10.1109/OJUFFC.2025.3577590

Volumetric Passive Ultrasound Localization Microscopy of Radiation-Induced Nanodroplet Vaporization With a Large Aperture Matrix Array

SOPHIE V. HEYMANS[1,2] (Member, IEEE), MARCUS INGRAM[1], BRAM CARLIER[3], BRECHT VANDENBORRE[2], MARC FOURNELLE[4] (Member, IEEE), ALESSANDRO RAMALLI[5] (Senior Member, IEEE), FRANÇOIS ROTTENBERG[6] (Member, IEEE), KOEN VAN DEN ABEELE[2], AND JAN D'HOOGE[1] (Member, IEEE)

[1]Department of Cardiovascular Sciences, KU Leuven, 3000 Leuven, Belgium
[2]Department of Physics, KU Leuven, 8500 Kortrijk, Belgium
[3]Department of Imaging and Pathology, KU Leuven, 3000 Leuven, Belgium
[4]Fraunhofer-Institut für Biomedizinische Technik (IBMT), Sankt Ingbert, 66386 Saarland, Germany
[5]Department of Information Engineering, University of Florence, 50139 Florence, Italy
[6]Department of Electrical Engineering, KU Leuven, 9000 Ghent, Belgium

CORRESPONDING AUTHOR: S. V. HEYMANS (sophie.heymans@kuleuven.be)

This work was supported by the Research Foundation Flanders. The work of Sophie V. Heymans was supported by the Junior Postdoctoral Fellowship under Grant 12E0923N. The work of Bram Carlier was supported by the Ph.D. Fellowship Fundamental Research under Grant 11A9520N.

ABSTRACT Superheated nanodroplets (NDs) are proposed for *in vivo* radiation dose sensing applications, based on their ability to vaporize into echogenic microbubbles when exposed to ionizing radiation. Combined with Ultrasound Localization Microscopy (ULM), the ultrafast detection of radiation-induced ND vaporization produces super-resolved vaporization maps that match the radiation field with sub-millimeter accuracy. However, in the presence of flow, discriminating between microbubbles moving in the field of view and radiation-induced vaporization events is not trivial. As an alternative, sparse acoustic signatures emitted by vaporizing NDs can be super-localized by passive ULM, i.e. P-ULM. In this work, we extend our previous 2D implementation of P-ULM to 3D, using a large aperture matrix array probe. We exposed perfluorobutane NDs to a proton beam and recorded their vaporization signatures during irradiation. The events were extracted from the radiofrequency channel data using a spatiotemporal filtering approach and super-localized by fitting the time differences of arrival between channels to a one-way time of flight model. The vaporization maps were overlaid on the proton beam distribution and estimated the proton range and beam dispersion within 0.98 ± 0.04 mm and 0.03 ± 0.02 mm of the reference range measurement (depth-dose distribution in water measured with a diode), respectively. These results pave the way for volumetric dose mapping using radiosensitive nanodroplets and passive imaging.

INDEX TERMS Nanodroplets, passive source localization, phase change contrast agents, proton range verification, radiation dosimetry, ultrasound localization microscopy, volumetric ultrasound.

I. INTRODUCTION

RADIOTHERAPY is an essential pillar in the management of cancer. When radiation beams are optimally conformed to the tumor geometry, maximal damage to the tumor can be achieved with minimal dose to surrounding healthy tissues. To manage potential target motion and uncertainties in dose delivery, real-time image guidance combined with *in vivo* dosimetry is desired [1]. This is even more critical for proton therapy, due to the high dose gradients of the Bragg peak and the finite, tunable range of protons in tissue [2].

Ultrasound (US) imaging of radiosensitive contrast agents was recently proposed for *in vivo* radiation dosimetry. Superheated nanodroplets (NDs) vaporize into echogenic microbubbles upon exposure to proton radiation, enabling US-based proton range verification [3]. The sensitivity to ionizing radiation was found to increase with the degree of superheat of the ND liquid core, and with the linear energy transfer (LET), *i.e.* the density of energy deposition per unit length, of charged particles [4]. Extending the current concept to volumetric US imaging would facilitate 3D dosimetry with real-time motion management during radiotherapy delivery.

For typical dose rates used in proton therapy, sparse ND vaporizations can be detected by high frame rate US imaging. Hence, by combining differential imaging and super-resolution localization of individual microbubbles, Ultrasound Localization Microscopy (ULM) [5], [6] can be applied to build super-resolved maps of ND vaporization events. Although we previously applied 2D ULM for NDs immobilized in gel phantoms [7], transitioning to more realistic physiological flow was hindered by the need to distinguish between vaporization events and existing microbubbles flowing in and out of the field of view. As a solution, we proposed to passively detect the acoustic signatures of volumetric oscillations generated by vaporizing NDs [8]. By detecting sparse events and localizing their position using a time-difference of arrival (TDoA) model, the passive ULM (P-ULM) technique was able to reconstruct the ND vaporization spatial distribution in flow phantoms [9].

Here, we extend our existing 2D P-ULM solution to 3D, motivated by the clinical need for a volumetric assessment of the radiation dose. We passively recorded acoustic signatures of NDs vaporized by a proton beam, using a wide aperture 11 × 11 matrix array. Individual vaporizations were super-localized and compared to the proton beam distribution in order to determine the performance of P-ULM for proton range verification.

II. MATERIALS AND METHODS

A. P-ULM PRINCIPLE AND THEORETICAL RESOLUTION LIMITS

As a continuous proton beam is used, ND vaporizations occur continuously throughout irradiation, at a rate determined by the likelihood of a proton or high-LET particle to stop in the ND liquid core [10]. In the absence of a time reference, ND vaporizations are localized using the TDoAs between channels:

$$\Delta\tau_i = \frac{\sqrt{(x_i - x_0)^2 + (y_i - y_0)^2 + z_0^2}}{c} - \frac{\sqrt{\left(x_{ref} - x_0\right)^2 + \left(y_{ref} - y_0\right)^2 + z_0^2}}{c} + \varepsilon \quad (1)$$

with (x_i, y_i) the azimuth and elevation coordinates of array element i, $\left(x_{ref}, y_{ref}\right)$ the coordinates of the reference channel, (x_0, y_0, z_0) the coordinates of the vaporization event, and c the speed of sound. An additional fitting variable, ε, is included to account for uncertainties in the estimation of the arrival time for the reference channel. Following the approach described in [11], and previously applied to 2D P-ULM [9], we determined the theoretical resolution limits for 3D P-ULM:

$$\sigma_{\hat{x_0}} \cong 2\sqrt{3}\sigma_{\Delta\tau} c z_0 \frac{\sqrt{L_x^4 + 60L_x^2 x_0^2 + L_y^4}}{L_x\sqrt{n\left(L_x^4 + L_y^4\right)}} \quad (2)$$

$$\sigma_{\hat{y_0}} \cong 2\sqrt{3}\sigma_{\Delta\tau} c z_0 \frac{\sqrt{L_x^4 + 60L_y^2 y_0^2 + L_y^4}}{L_y\sqrt{n\left(L_x^4 + L_y^4\right)}} \quad (3)$$

$$\sigma_{\hat{z_0}} \cong 12\sqrt{5}\sigma_{\Delta\tau} c \frac{z_0^2}{\sqrt{n\left(L_x^4 + L_y^4\right)}} \quad (4)$$

where n is the number of array elements, L_x and L_y are the array apertures in azimuth and elevation, respectively, and $\sigma_{\Delta\tau}$ is the uncertainty in the determination of the TDoAs.

B. EXPERIMENTAL METHODS

1) ND SYNTHESIS

Superheated NDs with a polyvinyl alcohol (PVA) shell and a perfluorobutane liquid core (PFB) were prepared following previously described protocols [4] and stored at 4°C for three days. Their size distribution was previously measured by Dynamic Light Scattering, yielding an intensity-weighted median diameter of 799 nm and polydispersity index of 0.3 [4]. The NDs PFB concentration was quantified on the day of the irradiation experiment using Nuclear Magnetic Resonance spectroscopy (400 MHz Avance II, Bruker Biospin GmbH, Rheinstetten, Germany).

2) EXPERIMENTAL SETUP AND IRRADIATION SETTINGS

Proton irradiations were performed at the Cyclotron Resource Center (UCLouvain, Louvain-la-Neuve, Belgium), using a passively scattered proton beam of 62 MeV and collimated with a circular brass collimator of 15 mm diameter (Fig. 1). The proton beam was aligned to enter a polymethyl methacrylate sample container (inner dimensions 85 × 70 × 80 mm^3) containing deionized water heated to 50°C in which NDs were diluted to a concentration of 50 μM and stirred with a magnetic stirrer at a speed of 250 rpm. Three samples were irradiated with a dose rate of 1 Gy/s and received a total dose of 4 Gy (reported at the Bragg peak). After irradiation, the sample container was flushed and refilled. For each irradiation, the proton flux was measured with an ionization chamber positioned in the beam line to determine the exact dose received by each sample.

3) PASSIVE ACQUISITION SETTINGS

An 11 × 11-element 2 MHz matrix array probe with 2.56 mm^2 square elements, for a total aperture of 30.9 mm^2 [12] (Fraunhofer IBMT, Germany), was positioned with its azimuth axis parallel to the proton beam direction (Fig. 1) and coupled to the sample container by an

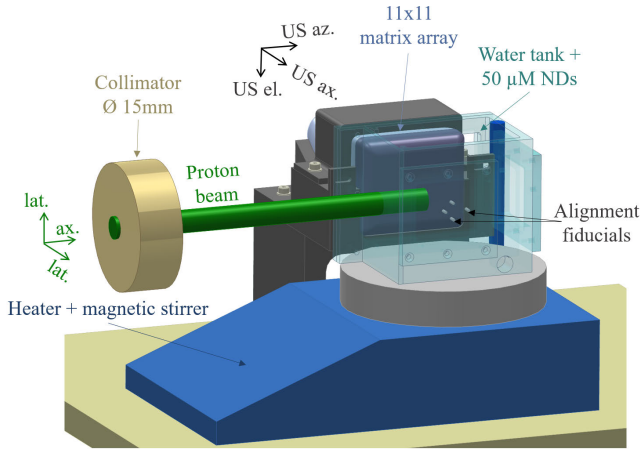

FIGURE 1. Experimental setup used for volumetric passive imaging of ND vaporization during proton irradiation.

acoustically-transparent window (20 μm-thick polyester film). The array was connected to an ULA-OP 256 research platform (X-Phase srl, Florence, Italy) [13] to passively acquire ND vaporization signals during irradiation. Passive radiofrequency (RF) frames of 419 μs duration were captured at 19.5 MHz sampling rate and 1 kHz repetition rate, using the maximum available gain (40 dB). The acoustic acquisition started one second before irradiation and lasted five seconds.

4) IMAGE REGISTRATION AND PROTON BEAM MODEL

Four screw fiducials were inserted into the opposite container wall to register the US coordinates to the room coordinates and correct for potential probe tilts (Fig. 1). The proton range in water was measured by scanning a dosimetry diode (PR60020, PTW, Freiburg, Germany) along the depth of the proton beam, with a 1 mm step size [14]. An analytic expression of the Bragg curve [15] was fitted to the measured depth-dose distribution to determine the proton range in water (distal 80% dose point, R_{80} [1]) and beam dispersion (σ_p). The range in the sample was obtained by including the water equivalent thickness of the entrance window [16]. The distributions of primary protons stopping due to Coulomb interactions and nuclear reactions were modelled as previously described [9]. The entrance beam diameter was set to the collimator diameter and beam spreading was modelled by the Highland formula [17], [18].

C. DATA PROCESSING AND ANALYSIS

1) P-ULM PIPELINE

The acquired RF data were processed in Matlab (R2024a, The Mathworks, Natick, MA, USA). The RF data were band-pass filtered (150 kHz - 3 MHz, infinite impulse response Butterworth filter, order 6) to remove frequencies outside the expected bandwidth of the vaporization signals. In addition, we implemented a spatiotemporal filter which is briefly described below. For every frame, the RF data is represented by the tall $Z \times N_{el}$ ($Z > N_{el}$) matrix $\mathbf{S}_{n+v}$, where Z is the number of axial time samples, N_{el} is the number of array elements, and the subscript indices n and v represent noise and vaporization signals, respectively. The frames $\boldsymbol{S_n}$ acquired before the start of irradiation are assumed to contain only noise, and can be decomposed using a Singular Value Decomposition (SVD):

$$\boldsymbol{S_n} = \boldsymbol{U_n}\begin{pmatrix}\boldsymbol{\Delta_n}\\ \mathbf{0}\end{pmatrix}\boldsymbol{V_n^t} \tag{5}$$

The matrices $\boldsymbol{U_n}$ and $\boldsymbol{V}_n$ are orthonormal matrices of dimensions ($Z \times Z$) and ($N_{el} \times N_{el}$), respectively, and $\boldsymbol{\Delta_n}$ is a diagonal matrix containing the singular values sorted in decreasing order. Assuming that the noise is highly correlated in time and space, we decompose the noise space into a low rank subspace (subscript 1) and null subspace (subscript 0):

$$\begin{aligned}\boldsymbol{S_n} &= \boldsymbol{U_n}\begin{pmatrix}\boldsymbol{\Delta_n}\\ \mathbf{0}\end{pmatrix}\boldsymbol{V_n^t} = \begin{pmatrix}\boldsymbol{U_{n,1}} & \boldsymbol{U_{n,0}}\end{pmatrix}\begin{pmatrix}\Delta_1 & 0\\ 0 & 0\end{pmatrix}\begin{pmatrix}V^t_{n,1}\\ V^t_{n,0}\end{pmatrix}\\ &= \boldsymbol{U_{n,1}\Delta_1 V^t_{n,1}}\end{aligned} \tag{6}$$

Assuming that: (i) the noise and vaporization signals are linearly superposed, i.e. $\boldsymbol{S_{n+v}} = \tilde{\boldsymbol{S}}_n + \boldsymbol{S_v}$ and (ii) the statistics of the noise are stationary, i.e. $\tilde{S}_n$ has the same SVD basis so that $\widetilde{\boldsymbol{S_n}} = \boldsymbol{U_n}\begin{pmatrix}\widetilde{\boldsymbol{\Delta_n}}\\ \mathbf{0}\end{pmatrix}\boldsymbol{V_n^t}$, we filter the signal as follows:

$$\begin{aligned}\boldsymbol{S_f} &= \boldsymbol{U_{n,0}U^t_{n,0}S_{n+v}V_{n,0}V^t_{n,0}} = \boldsymbol{U_{n,0}U^t_{n,0}S_vV_{n,0}V^t_{n,0}}\\ &+ \boldsymbol{U_{n,0}U^t_{n,0}U_{n,1}\widetilde{\Delta}_1 V^t_{n,1}V_{n,0}V^t_{n,0}}\end{aligned} \tag{7}$$

As the columns of $\boldsymbol{U_n}$ and $\boldsymbol{V_n}$ are orthogonal, the second term of the right side of equation (7) cancels. Assuming that the desired signal lies in the noise null subspace, we further find that the recovered vaporization signals are unaltered by the filter, i.e. $\boldsymbol{S_f} \cong \boldsymbol{S_v}$.

In practice, we estimate the matrices $\boldsymbol{U_n}$ and $\boldsymbol{V_n}$ by performing an eigenvector decomposition on the spatial and temporal covariance matrices $\boldsymbol{S_nS^t_n}$ and $\boldsymbol{S^t_nS_n}$ [19], respectively, averaged across all frames $\boldsymbol{S_n}$ acquired before the start of irradiation. The cutoff between the low rank noise subspace and null subspace was determined empirically by comparing the singular value amplitudes of frames acquired before irradiation ($\boldsymbol{\Delta_n}$) and during irradiation ($\boldsymbol{\Delta_{n+v}}$). As the presence of vaporization signals did not affect the first eight singular values (relative change in singular value amplitude $<$10%), we chose these singular values to determine $\boldsymbol{\Delta_1}$. Additional 2D Wiener filters (kernel size [18 3]) were applied in the Z-X and Z-Y dimensions to further denoise the RF data.

Candidate vaporization signals were detected on the filtered RF data $\boldsymbol{S_f}$ by computing the signal energy over short windows (39 μs, 85 % overlap) and retaining peaks superior to 4 standard deviations (std) above the mean energy of frames acquired prior to irradiation. Next, candidate signals were cropped and upsampled ($\times$10). For each candidate signal, a rectangular dense sub-array and reference channel were determined based on the signal to noise ratio (SNR) of the array rows and columns. The signals

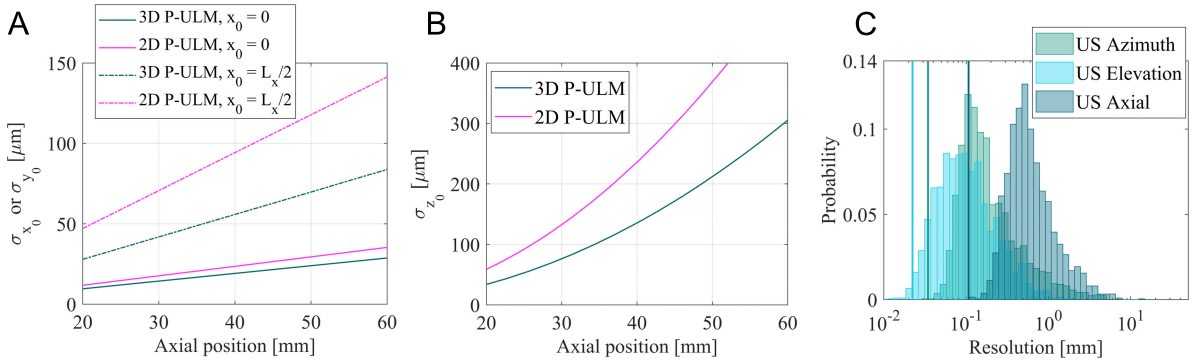

FIGURE 2. (A-B) Theoretical resolution limits of 3D P-ULM in the azimuth/elevation US direction (A) and axial US direction (B) as a function of the axial vaporization event position. The limits (in the US azimuth and axial direction) are compared to a reference 2D P-ULM situation (same array aperture, λ/2 pitch). (C) Distribution of the experimental resolution of individual vaporization events for one sample. The vertical lines represent the median resolution that would have been achieved by using all array elements.

of every sub-array channel were cross-correlated to the reference channel signal to determine the TDoAs. The latter were fitted to equation (1) with a two-step non-linear least squares curve fitting approach previously described in [9]. Only vaporization signals with a coefficient of determination (r^2) above 0.97 were kept. NDs acoustic signatures were obtained via coherently summing the channel data using the fitted TDoAs; their center frequency was computed as the mean frequency of the Fourier spectrum, and their SNR was calculated as the maximum amplitude of the signal envelope divided by the standard deviation of the background noise.

2) EXPERIMENTAL RESOLUTION LIMITS

The experimental error in the estimated TDoAs of every localized event was assessed as the std, $\sigma_{\Delta\tau,exp}$, of the residuals of the non-linear least squares curve fit. This experimental error was substituted in equations 2-4 together with the known speed of sound, event coordinates, and sub-array settings used for localization, in order to determine the resolution limits for every event. The fitted event position was then convolved with a 3D Gaussian kernel with std set to the expected resolution limit of this particular event in all three directions. To ensure every vaporization equally contributed to the resulting image, the total energy of the Gaussian convolved with every localization was kept fixed.

3) COMPARISON WITH PROTON BEAM SPATIAL DISTRIBUTION

The resulting vaporization map was compared to the proton beam spatial distribution in every direction by integrating along the remaining two directions to create 1D profiles. The proton range, $R_{80,exp}$, was estimated by fitting the vaporization profile to a linear combination of the primary protons stopping distribution and the nuclear reaction distribution [10]. The number of vaporizations due to nuclear reactions and primary protons were extracted from this fit, and the latter was normalized to the number of primary protons stopping in the Bragg peak and the ND concentration, as in [10]. The beam dispersion $\sigma_{p,exp}$ was estimated by applying a 1D Gaussian fit to the vaporization profile [10].

III. RESULTS

The median experimental error in the estimated TDoAs, $\sigma_{\Delta\tau,exp}$, was 30.2 ns. Figs. 2A and B compare the theoretical resolution limits in the azimuth/elevation and axial direction, respectively, substituting $\sigma_{\Delta\tau,exp}$ and the matrix array parameters in equations 2-4. For comparison, we also show the 2D resolution limits for a 1D array of same aperture (L_x = 30.9 mm) and λ/2 element pitch. The mean center frequency of individual acoustic signatures was 0.78 MHz (range 0.33 – 1.8 MHz), and the SNR increased from 14.3 ± 2.7 to 38.9 ± 3.6 dB after filtering. The histogram distribution of the experimental resolution of the localized events is shown in Fig. 2C (median values averaged across the samples are 166 μm, 92 μm and 574 μm in the US azimuth, elevation and axial directions, respectively). The number (mean ± std) of sub-array elements retained for TDoAs determination was 36 ± 15 (with a minimum of 10 elements); this corresponded to an aperture length of 17.5 ± 5 mm in azimuth and elevation.

Fig. 3A represents the 3D spatial distribution of the localized vaporization events for a single sample, overlaid on the proton stopping distribution. As observed in previous studies, at 50°C, ND vaporization is mostly triggered by primary protons stopping at the Bragg peak, while a lower density of ND vaporizations proximal to the Bragg peak can be attributed to vaporization by secondary particles generated by nuclear reactions [4], [7], [10]. We localized ~2400 events at a 4 Gy peak dose, with 68% occurring in the Bragg peak. The normalized number of events in the Bragg peak was 13.8 ± 1.7 per 10^8 protons and per μM NDs (3 samples). Fig. 3B-C shows the 1D profiles extracted from the vaporization map.

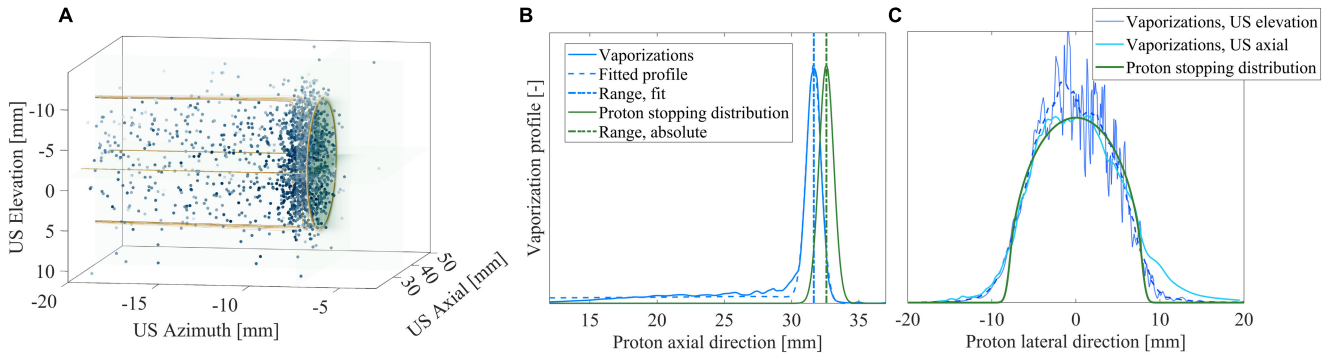

FIGURE 3. **A) 3D distribution of vaporization events localized during irradiation of a sample containing 50 μM NDs. The blue dots represent individual vaporization events (darker to lighter blue represent better to worse spatial resolution). The green color map represents the distribution of protons stopping due to Coulomb interactions, and brown contours show the distribution of protons stopping due to nuclear reactions. B) and C) 1D profiles of the vaporization events in the proton axial (US azimuth) and proton lateral (US elevation and axial) directions, respectively. In the US elevation direction (C), the dashed blue line represents the smoothing of the vaporization profile by an additional moving average filter.**

The estimation error was 0.98 ± 0.04 mm for the proton range ($R_{80} - R_{80,exp}$) and -0.03 ± 0.02 mm for the beam dispersion ($\sigma_p - \sigma_{p,exp}$).

IV. DISCUSSION AND CONCLUSION

These results show that volumetric P-ULM can localize ND vaporizations with a lateral resolution one order of magnitude below the diffraction limit, as demonstrated by the ability to recover the beam dispersion ($\sigma_p = 0.54$ mm) with an error < 0.03 mm. As a comparison, the diffraction-limited point spread function was reported to be $\sim$2.5 mm in azimuth and elevation, for a similar depth range [12]. We attribute the 0.98 mm shift in measured proton range to uncertainties in the absolute range measurement ($\pm$ 0.5 mm) and in the translation from US to room coordinates ($< \pm 1$ mm). Nevertheless, this error remains below the range uncertainty margins typically applied to proton therapy treatment plans [1], highlighting the potential for range verification. Co-registration of passive vaporization maps with volumetric ultrasound images would further enable the direct overlay of the proton range on the patient's anatomy.

As shown in Fig. 2A-B, besides enabling elevation localization, 3D P-ULM improves the theoretical resolution in the azimuth and axial US directions, compared to a similar 2D P-ULM configuration. Due to the low SNR, sub-arrays were used to fit the TDoAs, yielding a spatial resolution $\sim$5 times above the resolution achievable with all elements (Fig. 2C). The experimental resolution was better in the elevation US direction than in the azimuth US direction as the Bragg peak was off-center (~ -8 mm) in azimuth. In the axial US direction, a wider penumbra was observed at large depths (Fig. 3C), which we attribute to the worsening of the axial resolution with the square of the depth (equation 4). Despite the wider array aperture, we achieve similar experimental resolution limits in the azimuth and axial direction compared to our previous 2D P-ULM study [9], presumably due to the higher $\sigma_{\Delta\tau,exp}$ and use of sub-arrays for localization. Future research will aim at improving the SNR using bespoke probes and exploring passive beamforming methodologies to exploit the signals received by all array elements.

The normalized number of localized events (13.8 ± 1.7) closely matched the expected value of 15.7 events per 10^8 protons in the Bragg peak and per μM NDs predicted by our analytical model [10], which assumes that the number of vaporizations due to primary protons is proportional to the numbers of primary protons stopping in the Bragg peak and the volume concentration of perfluorocarbon liquid in the sample. This value is also similar to the normalized vaporization yield observed in the previous 2D P-ULM study ($\sim$12 events), when accounting only for protons stopping within the $-$ 6 dB elevation beam width (estimated to be 4.3 mm using Field II simulations [20]). In our configuration, for the same proton dose, transitioning from 2D to 3D P-ULM multiplies the number of localized events by 2.9 through the increase in elevation beam width, thereby enhancing the achievable accuracy for range verification. Moreover, importantly, 3D P-ULM eliminates the localization biases caused by the violated $y_0 = 0$ assumption in the 2D TDoA model. These previously resulted in a 1 mm discrepancy between the axial positions of vaporization events in 2D ULM and 2D P-ULM [9]. Finally, the use of 3D P-ULM allows monitoring of scanned proton beams (delivered by most clinical proton therapy systems), which would be impossible with 2D P-ULM as the array elevation position needs to coincide with the proton beam axis.

Due to the polydispersity of the ND population, a broad variability in the frequency of the vaporization signals was observed, as the latter is related to the size of the resulting microbubble [8]. Most vaporizations had a center frequency outside of the -6 dB bandwidth of the array (1.3 – 2.7 MHz). The observed mean center frequency is lower than that reported in our previous 2D P-ULM study (1.5 MHz) [9]; we attribute this apparent difference to the different array and filtering approach. ND size sorting could be explored

to tune the ND vaporization signal frequency to the array bandwidth.

A limitation of this study is the use of a temperature of 50°C, chosen to achieve sensitivity to primary protons with a C_4F_{10} ND formulation [4]. A similar response could be obtained at body temperature by using NDs with a more volatile core (such as C_3F_8) and/or composite cores [21], or by applying acoustic modulation to increase the ND degree of superheat at body temperature [22]. The localization performance and sensitivity of volumetric P-ULM should also be validated *in vivo* in future studies, as vaporization dynamics may differ [23]. Additionally, vaporization signals could be more strongly impacted by tissue attenuation and acoustic diffraction.

In conclusion, we presented a P-ULM approach enabling to super-localize sparse ND vaporizations in 3D. While we here demonstrate the performances of 3D P-ULM for proton range verification, this technique is not limited to radiation-induced vaporization and could apply to acoustic or optical vaporization of sparse NDs in a situation in which the vaporization time is unknown (*e.g.* long sonication). In the context of range verification, a comprehensive comparison of active and passive volumetric ULM would be of interest, as they might provide distinct advantages. This will be explored in future studies.

ACKNOWLEDGMENT

The authors thank the Cyclotron Resource Center (UCLouvain), the mechanical workshop of the Physics Department (KU Leuven), and Dr. Hewener and Dr. Weber (Fraunhofer IBMT) for their support with the matrix array used in this study.

REFERENCES

[1] H. Paganetti, "Range uncertainties in proton therapy and the role of Monte Carlo simulations," *Phys. Med. Biol.*, vol. 57, no. 11, pp. R99–R117, Jun. 2012, doi: 10.1088/0031-9155/57/11/r99.

[2] K. Parodi and J. C. Polf, "In vivo range verification in particle therapy," *Med. Phys.*, vol. 45, no. 11, pp. e1036–e1050, Nov. 2018, doi: 10.1002/mp.12960.

[3] B. Carlier et al., "Phase-change ultrasound contrast agents for proton range verification: Towards an in vivo application," *Phys. Med. Biol.*, vol. 69, no. 20, Oct. 2024, Art. no. 205014, doi: 10.1088/1361-6560/ad7e76.

[4] S. V. Heymans et al., "Modulating ultrasound contrast generation from injectable nanodroplets for proton range verification by varying the degree of superheat," *Med. Phys.*, vol. 48, no. 4, pp. 1983–1995, Apr. 2021, doi: 10.1002/mp.14778.

[5] C. Errico et al., "Ultrafast ultrasound localization microscopy for deep super-resolution vascular imaging," *Nature*, vol. 527, no. 7579, pp. 499–502, Nov. 2015, doi: 10.1038/nature16066.

[6] G. Zhang et al., "Acoustic wave sparsely activated localization microscopy (AWSALM): Super-resolution ultrasound imaging using acoustic activation and deactivation of nanodroplets," *Appl. Phys. Lett.*, vol. 113, no. 1, Jul. 2018, Art. no. 014101, doi: 10.1063/1.5029874.

[7] G. Collado-Lara et al., "Spatiotemporal distribution of nanodroplet vaporization in a proton beam using real-time ultrasound imaging for range verification," *Ultrasound Med. Biol.*, vol. 48, no. 1, pp. 149–156, Jan. 2022, doi: 10.1016/j.ultrasmedbio.2021.09.009.

[8] P. S. Sheeran, T. O. Matsunaga, and P. A. Dayton, "Phase change events of volatile liquid perfluorocarbon contrast agents produce unique acoustic signatures," *Phys. Med. Biol.*, vol. 59, no. 2, pp. 379–401, Dec. 2013, doi: 10.1088/0031-9155/59/2/379.

[9] S. V. Heymans et al., "Passive ultrasound localization microscopy of nanodroplet vaporizations during proton irradiation," *IEEE Open J. Ultrason., Ferroelectr., Freq. Control*, vol. 2, pp. 203–219, 2022, doi: 10.1109/OJUFFC.2022.3213534.

[10] G. Collado-Lara et al., "Analytic prediction of droplet vaporization events to estimate the precision of ultrasound-based proton range verification," *Med. Phys.*, vol. 50, no. 7, pp. 4562–4577, Jul. 2023, doi: 10.1002/mp.16327.

[11] Y. Desailly, J. Pierre, O. Couture, and M. Tanter, "Resolution limits of ultrafast ultrasound localization microscopy," *Phys. Med. Biol.*, vol. 60, no. 22, pp. 8723–8740, Nov. 2015, doi: 10.1088/0031-9155/60/22/8723.

[12] H. J. Hewener, W. Bost, D. Speicher, M. Ehrhardt, M. Fournelle, and S. Tretbar, "Low-cost, volumetric imaging with large footprint 11×11-element matrix array probe on a 128 channel ultrasound research scanner," *Proc. Meetings Acoust.*, vol. 38, no. 1, 2019, Art. no. 020008, doi: 10.1121/2.0001088.

[13] E. Boni et al., "Architecture of an ultrasound system for continuous real-time high frame rate imaging," *IEEE Trans. Ultrason., Ferroelectr., Freq. Control*, vol. 64, no. 9, pp. 1276–1284, Sep. 2017, doi: 10.1109/TUFFC.2017.2727980.

[14] B. Carlier et al., "Proton range verification with ultrasound imaging using injectable radiation sensitive nanodroplets: A feasibility study," *Phys. Med. Biol.*, vol. 65, no. 6, Mar. 2020, Art. no. 065013, doi: 10.1088/1361-6560/ab7506.

[15] T. Bortfeld, "An analytical approximation of the Bragg curve for therapeutic proton beams," *Med. Phys.*, vol. 24, no. 12, pp. 2024–2033, Dec. 1997, doi: 10.1118/1.598116.

[16] H. Sierra, M. Cordova, C.-S.-J. Chen, and M. Rajadhyaksha, "Confocal imaging–guided laser ablation of basal cell carcinomas: An ex vivo study," *J. Investigative Dermatol.*, vol. 135, no. 2, pp. 612–615, Feb. 2015, doi: 10.1038/jid.2014.371.

[17] H. Paganetti, *Proton Therapy Physics*. Boca Raton, FL, USA: CRC Press, 2019.

[18] B. Gottschalk, A. M. Koehler, R. J. Schneider, J. M. Sisterson, and M. S. Wagner, "Multiple Coulomb scattering of 160 MeV protons," *Nucl. Instrum. Methods Phys. Res. Sect. B: Beam Interact. With Mater. At.*, vol. 74, no. 4, pp. 467–490, Jun. 1993, doi: 10.1016/0168-583x(93)95944-z.

[19] C. Demené et al., "Spatiotemporal clutter filtering of ultrafast ultrasound data highly increases Doppler and fUltrasound sensitivity," *IEEE Trans. Med. Imag.*, vol. 34, no. 11, pp. 2271–2285, Nov. 2015, doi: 10.1109/TMI.2015.2428634.

[20] J. A. Jensen, "Field: A program for simulating ultrasound systems," in *Proc. 10th NORDICBALTIC Conf. Biomed. Imag.*, vol. 4, 1996, pp. 351–353.

[21] K. Riemer et al., "3D acoustic wave sparsely activated localization microscopy with phase change contrast agents," *Investigative Radiol.*, vol. 59, no. 5, pp. 379–390, May 2024, doi: 10.1097/rli.0000000000001033.

[22] S. V. Heymans et al., "Acoustic modulation enables proton detection with nanodroplets at body temperature," *IEEE Trans. Ultrason., Ferroelectr., Freq. Control*, vol. 69, no. 6, pp. 2028–2038, Jun. 2022, doi: 10.1109/TUFFC.2022.3164805.

[23] J. D. Rojas, M. A. Borden, and P. A. Dayton, "Effect of hydrostatic pressure, boundary constraints and viscosity on the vaporization threshold of low-boiling-point phase-change contrast agents," *Ultrasound Med. Biol.*, vol. 45, no. 4, pp. 968–979, Apr. 2019, doi: 10.1016/j.ultrasmedbio.2018.11.006.